The Astrophysical Journal, 731:9 (14pp), 2011 April 10 doi:10.1088/0004-637X/731/1/9

ICES IN THE QUIESCENT IC 5146 DENSE CLOUD

J. E. Chiar[1], Y. J. Pendleton[2], L. J. Allamandola[2], A. C. A. Boogert[3], K. Ennico[2], T. P. Greene[2], T. R. Geballe[4], J. V. Keane[5], C. J. Lada[6], R. E. Mason[4], T. L. Roellig[2], S. A. Sandford[2], A. G. G. M. Tielens[7], M. W. Werner[8], D. C. B. Whittet[9], L. Decin[10], and K. Eriksson[11]

[1] SETI Institute, Carl Sagan Center, 189 Bernardo Avenue, Mountain View, CA 94035, USA; jchiar@seti.org
[2] NASA Ames Research Center, MS 245-6, Moffett Field, CA 94035, USA
[3] IPAC, NASA Herschel Science Center, Mail Code 100-22, California Institute of Technology, Pasadena, CA 91125, USA
[4] Gemini Observatory, Northern Operations Center, 670 North A'ohoku Place, Hilo, HI 96720, USA
[5] Institute for Astronomy, 2680 Woodlawn Drive, Honolulu, HI 96822, USA
[6] Harvard-Smithsonian Center for Astrophysics, 60 Garden Street, Cambridge, MA 02138, USA
[7] Leiden Observatory, P.O. Box 9513, 2300 RA Leiden, The Netherlands
[8] Jet Propulsion Laboratory, California Institute of Technology, 4800 Oak Grove Drive, Pasadena, CA 91109, USA
[9] New York Center for Astrobiology, Department of Physics, Applied Physics & Astronomy, Rensselaer Polytechnic Institute, Troy, NY 12180, USA
[10] Instituut voor Sterrenkunde, Katholieke Universiteit Leuven, Celestijnenlaan 200D, 3001 Leuven, Belgium
[11] Department of Physics & Astronomy, Uppsala University, Box 515, 751 20 Uppsala, Sweden
Received 2010 December 20; accepted 2011 January 24; published 2011 March 17

ABSTRACT

This paper presents spectra in the 2 to 20 μm range of quiescent cloud material located in the IC 5146 cloud complex. The spectra were obtained with NASA's Infrared Telescope Facility SpeX instrument and the *Spitzer Space Telescope*'s Infrared Spectrometer. We use these spectra to investigate dust and ice absorption features in pristine regions of the cloud that are unaltered by embedded stars. We find that the H_2O-ice threshold extinction is 4.03 ± 0.05 mag. Once foreground extinction is taken into account, however, the threshold drops to 3.2 mag, equivalent to that found for the Taurus dark cloud, generally assumed to be the touchstone quiescent cloud against which all other dense cloud and embedded young stellar object observations are compared. Substructure in the trough of the silicate band for two sources is attributed to CH_3OH and NH_3 in the ices, present at the $\sim$2% and $\sim$5% levels, respectively, relative to H_2O-ice. The correlation of the silicate feature with the $E(J - K)$ color excess is found to follow a much shallower slope relative to lines of sight that probe diffuse clouds, supporting the previous results by Chiar et al.

Key words: astrochemistry – dust, extinction – infrared: ISM – ISM: individual objects (IC 5146) – ISM: molecules

Online-only material: color figures

1. INTRODUCTION

Ices are abundant in preplanetary material and their presence is likely to represent a vital resource for the origin of planetary life (e.g., Mottl et al. 2007). Ices are widely observed in the dense molecular clouds that give birth to new stars (e.g., Gibb et al. 2004); they are ubiquitous in comets (e.g., Whipple 1950; Schulz et al. 2006) and have recently been detected on asteroidal bodies as well (Campins et al. 2010; Rivkin & Emery 2010). To determine the evolution of such materials, from icy coatings on submicron-sized interstellar grains to planetesimals in protoplanetary disks, is a major goal in the astronomical search for origins. A crucial first step is the formation of ice mixtures composed primarily of H_2O, CO, and CO_2 in molecular clouds. The observed abundances of these molecules in the solid phase can be explained by simple grain surface reactions such as $O + H \rightarrow OH$, $OH + H \rightarrow H_2O$, and $CO + OH \rightarrow CO_2 + H$, in combination with direct freeze-out of CO from the gas phase.

The physical conditions under which these reactions occur may vary from cloud to cloud, as a function of factors such as the cloud mass, temperature, and the intensity of the local interstellar radiation field. Ices are quite widely observed in the spectra of young stellar objects (YSOs), but the study of ices in pristine *prestellar* dark clouds requires observations of background field stars in lines of sight that do not intercept circumstellar material around YSOs. Relatively few such observations are currently available. The dark cloud in Taurus is by far the best studied to date (e.g., Whittet et al. 1988, 2007; Chiar et al. 1995; Bergin et al. 2005; Shenoy et al. 2008) and is often assumed to be prototypical, but this remains to be confirmed. Observations of ices toward a significant sample of background stars are available for only two other molecular clouds: Serpens and ρ Oph (Eiroa & Hodapp 1989; Tanaka et al. 1990; Chiar et al. 1994; Knez et al. 2005). Boogert et al. (2011) present a study of ices and extinction toward 16 isolated cores as probed by background stars and find the threshold extinction to be in line with that found in Taurus. The observations show similarities but also significant differences in ice properties and the conditions needed for ice to form. These differences may be parameterized in terms of the ice "extinction threshold," i.e., the minimum observed continuum extinction necessary for the detection of the ices (e.g., Whittet 2003), and in the relative abundances of H_2O, CO, and CO_2 (Whittet et al. 2007, 2009). To establish a reliable benchmark for studies of ice evolution in regions of active star formation, it is vital to understand the initial conditions in quiescent clouds and the extent to which they vary from cloud to cloud.

With this goal in mind, we present new observations of ices in the IC 5146 dark cloud complex. IC 5146 is nearly 3° in extent, located in the direction of Cygnus (Elias 1978; Dobashi et al. 1992). The IC 5146 complex consists of several dark clouds as well as the well-known H II region, the Cocoon Nebula (Dobashi et al. 1992). The dark cloud called the Northern

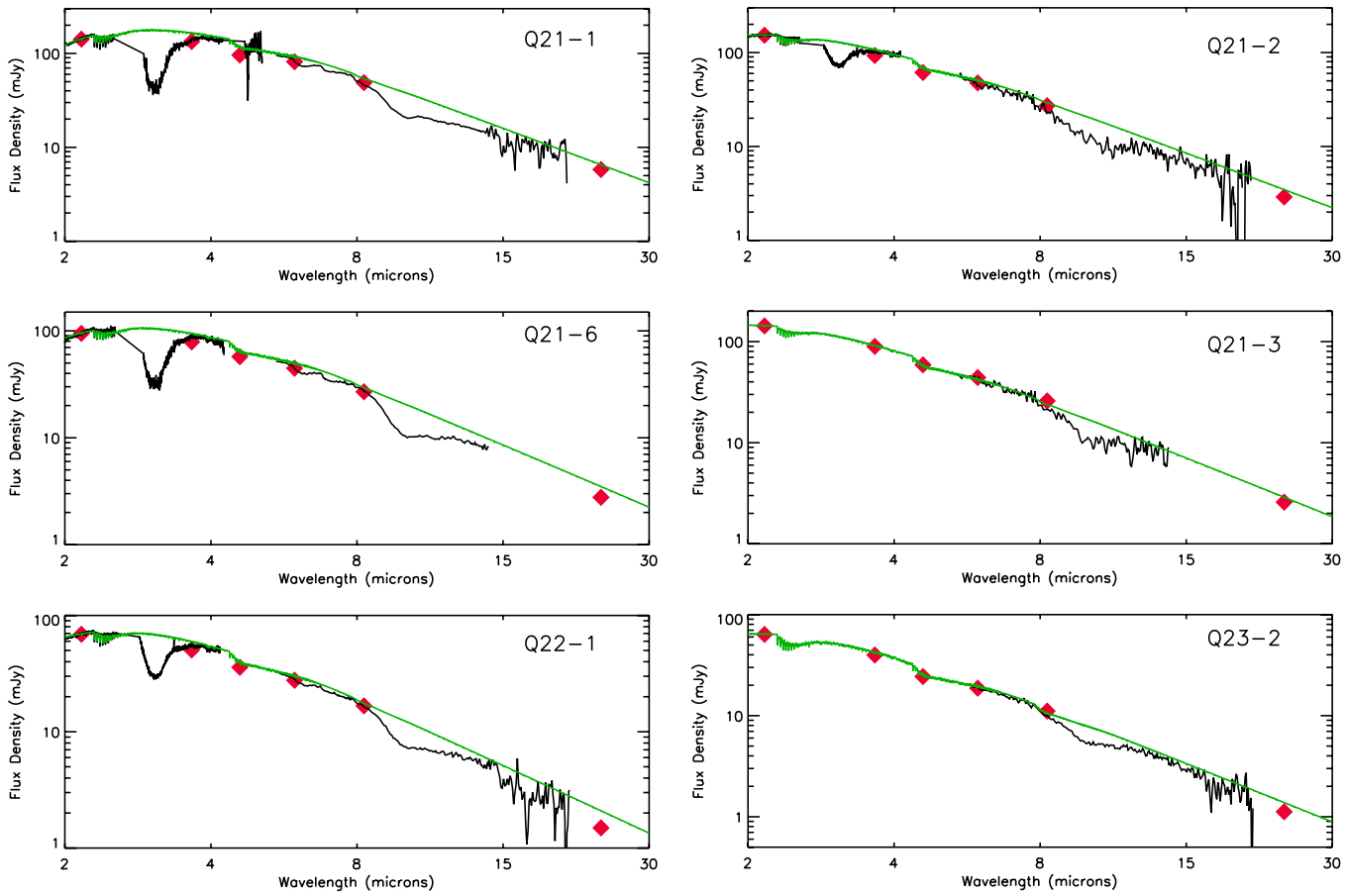

Figure 1. Spectral energy distributions for the IC 5146 field stars. 2MASS and IRAC photometry (diamonds), SpeX and IRS spectra (black lines), and the reddened photospheric model spectrum (green line) are shown. The spectra are plotted in order of decreasing visual extinction: Q21-1 ($A_V = 23.9$ mag), Q21-6 ($A_V = 20.7$ mag), Q22-1 ($A_V = 17.49$ mag), Q21-2 ($A_V = 12.2$ mag), Q21-3 ($A_V = 11.1$ mag), Q23-2 ($A_V = 10.1$ mag), Q21-4 ($A_V = 8.5$ mag), Q21-5 ($A_V = 8.0$ mag), Q23-1 ($A_V = 7.4$ mag), and Q22-3 ($A_V = 3.7$ mag).

(A color version of this figure is available in the online journal.)

Streamer, a region of high extinction compared to the rest of the cloud, is located to the west of the Cocoon (Cambrésy 1999; Lada et al. 1999; Harvey et al. 2008). It contains several protostellar clumps, some of which are actively forming stars (Dobashi et al. 1992). These distinct regions are thought to be co-distant at 950 pc (Harvey et al. 2008). Star formation in the H II region is loosely clustered and more efficient than that in the Northwest Streamer where most of the YSOs have formed in isolation. The field stars presented in this paper probe this relatively quiescent Northwest Streamer region. In Section 2, we describe the complete data set for the IC 5146 cloud including the *Spitzer* (IRS, IRAC, and MIPS), Two Micron All Sky Survey (2MASS; Skrutskie et al. 2006), and IRTF-SpeX observations. We used our IRTF-SpeX spectra to classify the spectral types of the background stars (Section 2.1), thus allowing us to fit the continuum flux using a reddened photospheric model appropriate for the spectral type of the star (Section 2.2). The resulting optical depth profiles and ice abundances are discussed in Section 3. The relationship between the near-infrared color excess and the silicate optical depth is discussed in Section 4. Finally, we summarize our results in Section 5.

2. OBSERVATIONS AND DATA REDUCTION

We used the Infrared Spectrometer (Houck et al. 2004) on the *Spitzer Space Telescope* (Werner et al. 2004) to obtain data in the 5 to 20 μm region of 10 sources behind the IC 5146 dark cloud, with visual extinction (A_V) in the range from 4 to 27 mag. Source names, 2MASS IDs, spectral class (see Section 2.1), extinction information, and AOR keys are listed in Table 1. The Infrared Spectrometer (IRS) pipeline version used was 15.3. The low-resolution Short-Low (SL) and Long-Low (LL) modules ($R \sim 60$–120) were reduced in a way that is customary for ground-based spectra, following the method described in Boogert et al. (2008). For the IC 5146 cloud, the background is relatively uniform across the array, so background subtraction was carried out by using the nodded pairs. A fixed width extraction was performed and the one-dimensional spectra were then averaged. Subsequently, the IC 5146 spectra were divided by the ratioed spectra of the standard stars HR 2194 (A0 V; PID 1417; AOR keys 0013024512 and 0013024768 for SL1 and SL2, respectively) and HR 6606 (G9 III; PID 1421; AOR key 0013731840 for LL) reduced in the same way in order to correct for wavelength-dependent slit losses. The standard stars were ratioed with the model spectra from Decin et al. (2007) appropriate for their spectral type.

For seven of these sources, we also obtained 1.9 to 4.0 μm data with the SpeX instrument (Rayner et al. 2003) on NASA's Infrared Telescope Facility (IRTF). The spectra were obtained using a 0.″8 slit with the long-wavelength cross-dispersed (LXD) mode of the SpeX instrument resulting in $R \sim 937$. The spectra were reduced using the SpeXtool software package (Vacca et al.

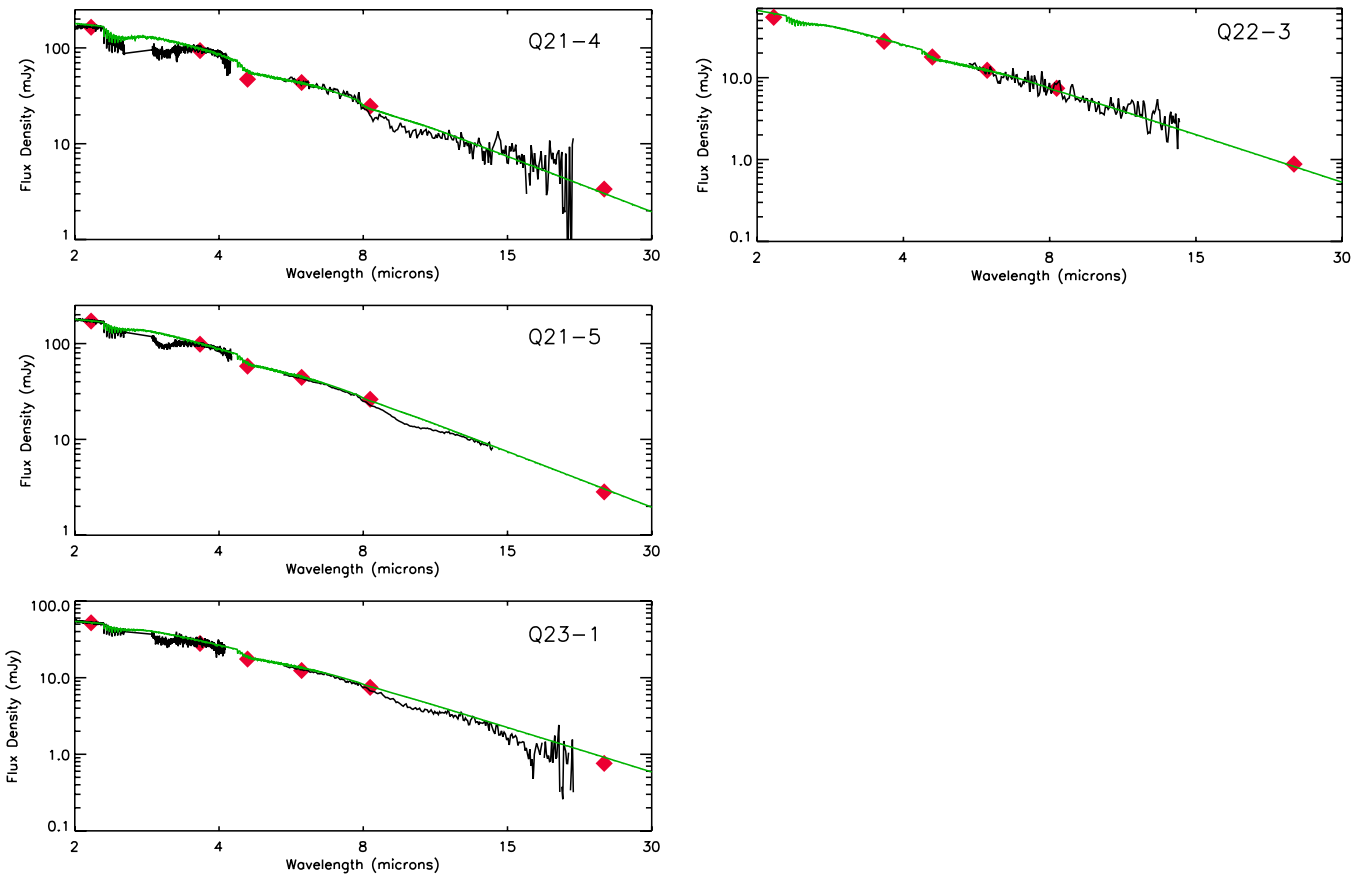

Figure 1. (Continued)

Table 1
Field Stars Located Behind IC 5146

2MASS ID	*Spitzer* AOR Label	Spectral Type[a]	$E(J-K)$[b]	A_V From Model Match	AOR Key
21472204+4734410	Q21-1	K2 III Fe-0.5	$4.5^{+0.07}_{-0.07}$	23.9	14136064
21463943+4733014	Q21-2	G8 III Fe-1	$2.3^{+0.05}_{-0.00}$	12.2	10750720
21475842+4737164	Q21-3	[K2 III]	2.1	11.1	10750720
21450774+4731151	Q21-4	K6 III CN 0.5	$1.6^{+0.08}_{-0.06}$	8.5	10750720
21444787+4732574	Q21-5	K2 III Fe-0.5	$1.5^{+0.07}_{-0.07}$	8.0	14136064
21461164+4734542	Q21-6	G8.5 IIIa Fe-0.5	$3.9^{+0.05}_{-0.00}$	20.7	14136064
21443293+4734569	Q22-1	K0 III	$3.3^{+0.04}_{-0.05}$	17.49	14136064
21473989+4735485	Q22-3	[K1 III]	0.7	3.7	10750976
21473509+4737164	Q23-1	K1 IIIb CN1.5 Ca1	$1.4^{+0.07}_{-0.04}$	7.4	14136064
21472220+4738045	Q23-2	[K5 III]	1.9	10.1	14136064

Notes.
[a] Spectral type based on match to standard-star spectra in IRTF Spectral Library, with reddening applied. Square brackets indicate that no IRTF data were available to classify the star and spectral type is based on the fit of reddened Decin models to photometry and *Spitzer* IRS spectra.
[b] Intrinsic colors from Tokunaga (2000).

2003; Cushing et al. 2004). These data were used to classify the spectral types of the stars and measure the 3.0 μm H_2O-ice absorption feature. For the most heavily obscured source Q21-1, we also obtained an *M*-band spectrum in order to measure the CO-ice profile at 4.67 μm.

In order to flux calibrate the *Spitzer*–IRS and IRTF-SpeX spectra, we used available photometry from 2MASS and IRAC (Harvey et al. 2008). The convolved flux at the effective wavelength of the photometric filter was calculated using published responsivity curves for 2MASS (Cohen et al. 2003) and IRAC (Reach et al. 2005). Following the calculation of the effective flux over a particular photometric passband, a normalization factor was calculated individually for the SpeX and IRS spectra. SpeX spectra were normalized to the 2MASS K_S band, and IRS spectra were normalized to either the IRAC3 or IRAC4 band. The flux calibrated spectra along with the photometry are shown in Figure 1.

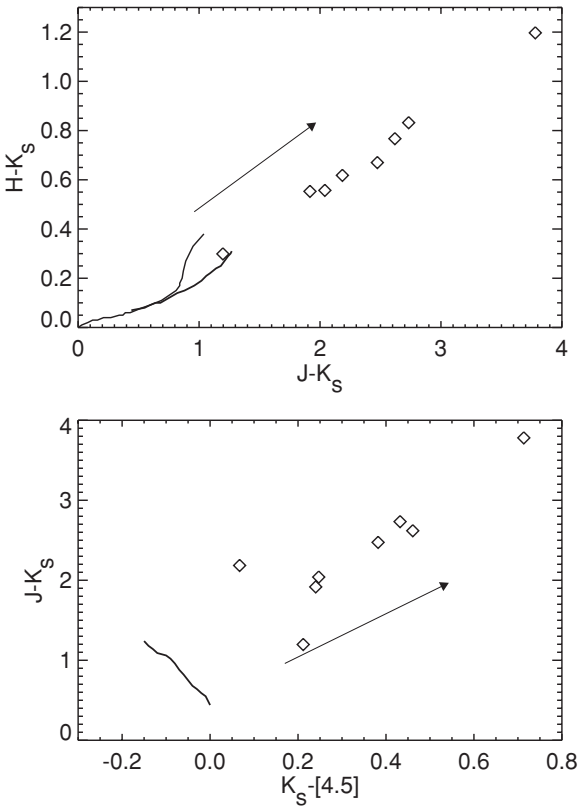

Figure 2. $H - K_s$ vs. J–K_s (top) and J–K_s vs. $K_s - [4.5]$ (bottom) for the IC 5146 field stars (diamonds). In the top panel, smooth lines denote the dwarf (upper curve) and giant (lower curve) branches of normal unreddened stars. In the bottom panel, the curve for normal giant stars is shown. The reddening vectors are equivalent to $A_V \sim 5$ mag.

2.1. Spectral Classification

In order to confirm the background nature of our sources, we constructed color–color diagrams which separate out reddened field stars from embedded objects and stars with circumstellar material. Figure 2 shows the placement of the IC 5146 sources with respect to normal giant and dwarf stars (Bessell & Brett 1988),[12] along with a reddening vector. Reddening curves are deduced using the extinction law determined by Indebetouw et al. (2005) and are equivalent to $A_V \sim 5$ mag. It is apparent from these diagrams that all the IC 5146 program stars are field giants reddened by dense cloud dust that displaces them from the red giant branch. YSOs and objects with circumstellar dust would fall near the bottom right in the $J - K_s$ versus $[4.5] - K_s$ diagram.

We used the 2.2 to 2.5 μm region to determine the spectral type of the stars for which we have IRTF-SpeX spectra (Figure 3). In this spectral region, the strength of the CO lines is a strong indicator of the spectral type (and luminosity class) of late-type stars. The ^{12}CO first overtone, spanning the 2.29–2.50 μm region, dominates the K-band spectra of the giant stars (Wallace & Hinkle 1996, 1997; Heras et al. 2002) and its strength increases with decreasing temperature (i.e., later spectral types). The 2–0, 3–1, and 2–4 bands of the ^{13}C^{16}O isotope are also present in these giant stars due to the larger CO absorption and decreased ^{12}C/^{13}C ratio (Wallace & Hinkle 1996). Additionally, the Ca multiplet and the Fe line in the 2.261–2.267 μm region strengthen somewhat in spectral types later than early G. The Mg line near 2.28 μm does not show much variation with temperature (Wallace & Hinkle 1996) and is present at similar strengths in all our spectra. In order to classify our background stars, we compared our observed spectra to the standard-star spectra available in the IRTF Spectral Library which contains 57 G0 through M10 giant-star spectra (Cushing et al. 2005; Rayner et al. 2009). The standard-star spectra were first reddened by applying the Indebetouw et al. (2005) extinction law from 1.25 to 8.0 μm, assuming constant extinction longward of 8 μm. We assume $A_K/A_V = 0.09$, appropriate for $R = 3.05$ (Whittet 2003). The visual extinction, A_V, was deduced based on $E(J - K)$, assuming average intrinsic colors for late G through early M giants from Tokunaga (2000) as a first best guess, and $A_V = 5.3 \times E(J - K)$, appropriate for dense clouds (Whittet et al. 2001). Using the deduced extinction curve and taking advantage of the sensitivity of the CO lines to temperature, we determined the spectral type for each source (Figure 3; Table 1). The uncertainty is no more than ± 1 in subtype. Following the classification, $E(J - K)$ was recalculated using the intrinsic colors for the appropriate spectral type; these values are given in Table 1.

2.2. Determination of Continuum and Optical Depth Profiles

The determination of an underlying stellar continuum is one of the biggest sources of uncertainty when deducing ice and dust absorption profiles. Polynomial continua are somewhat arbitrary, but are often used when the true stellar continuum is not known and/or cannot be easily modeled. Since we have photometry and spectroscopy over a wide wavelength region and we are able to determine the spectral types of our program stars with relative accuracy (Section 2.1), we are able to fit reddened photospheric models from Decin & Eriksson (2007). These models cover the spectral region from 2 to 40 μm and are available for K1, K2, and K5 giants. Thus, after the spectral type was determined based on the K-band spectrum, the Decin & Eriksson model closest to that spectral type was chosen. The model was reddened using the Indebetouw et al. (2005) extinction law as described above. After convolving the reddened model flux with the appropriate photometry point, the model was normalized to the data. In most cases, the reddened model was normalized to the K_s band, except for Q22-3 and Q21-4, where the IRAC4 and IRAC3 photometry, respectively, was used to normalize the reddened model. The reddened models provide reasonable continua over the entire spectral energy distribution (Figure 1). The optical depth spectra were computed using $\tau = -\ln F_\nu / F_{\rm continuum}$ and are presented in Figure 4.

3. ICE AND DUST ABSORPTION FEATURES

Several dust and ice absorption features are apparent in the optical depth spectra (Figure 4): the 3.0 μm H_2O-ice and associated wing, the 6.0 μm and 6.8 μm ice/dust features, and the 9.7 μm silicate feature. Figure 7 shows the CO-ice absorption profile for Q21-1.

3.1. H_2O-ice and Long-wavelength Wing

Water-ice is the primary ice-mantle constituent in dense clouds and its presence is evident through detection of its fundamental O–H stretching-mode absorption feature at 3.0 μm and bending and libration modes at 6.0 and 13 μm, respectively. In laboratory ice analogs, the peak depth of the 6.0 μm ice

[12] We chose not to transform these intrinsic colors to the 2MASS system because the transformation artificially displaces the "origin" of the dwarf branch away from $J - K_s = H - K_s = 0$.

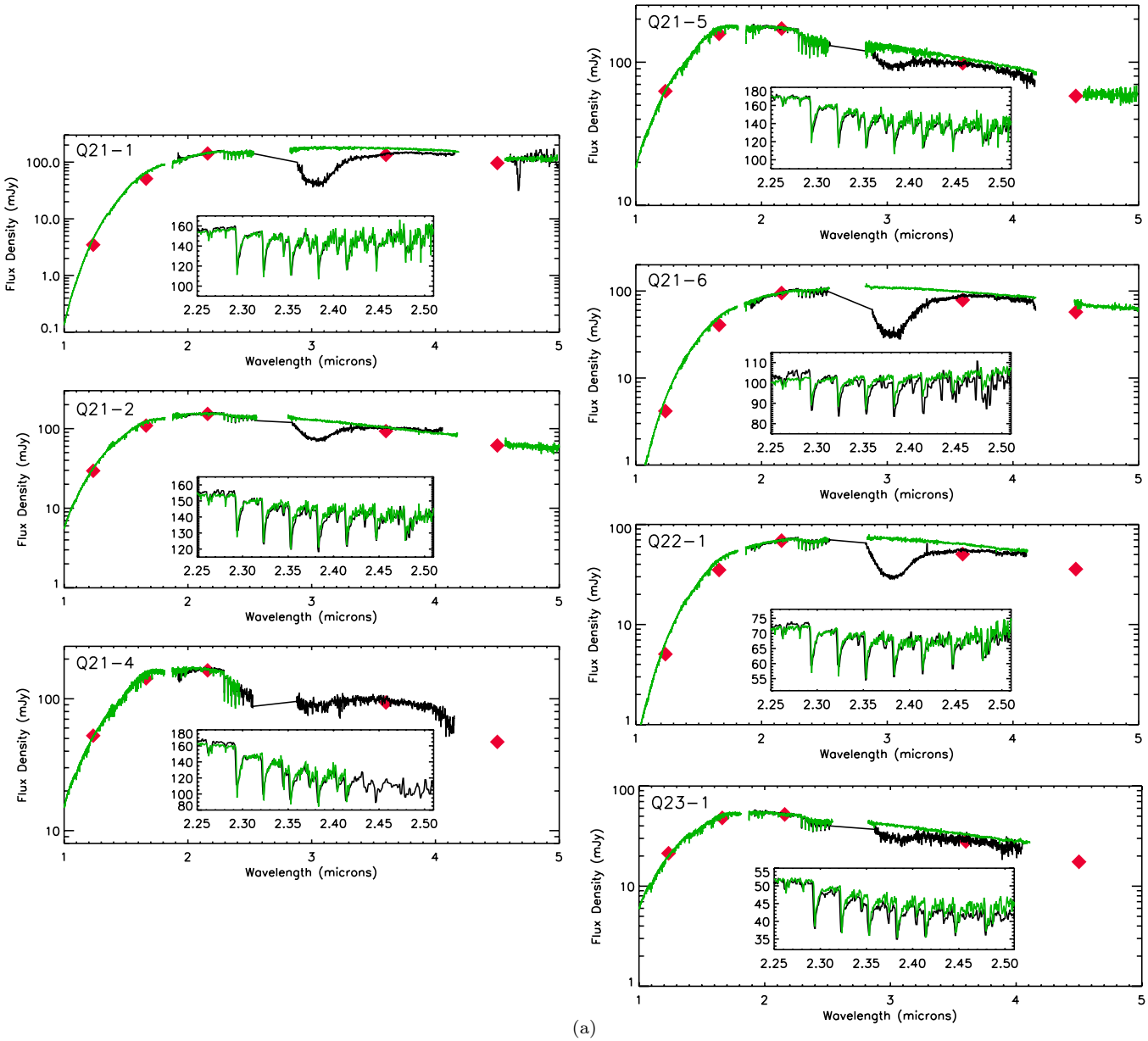

(a)

Figure 3. (a) Spectral energy distributions for the IC 5146 field stars with available IRTF-SpeX data. 2MASS photometry (diamonds), SpeX spectra of IC 5146 field star (black line), and SpeX standard star (green line). (b) IC 5146 field stars with no available SpeX data.

(A color version of this figure is available in the online journal.)

absorption feature is seven to nine times weaker than the 3.0 μm absorption, and in the astronomical spectra absorption at 6.0 μm is a blend of H_2O-ice with other ice components (see below). The libration band is also weak and blended on the shoulder of the broad 9.7 μm silicate absorption feature. The presence of alcohols and other compounds containing OH groups in the ice can contribute to the 3.0 μm absorption band and should be taken into account for those lines of sight that have CH_3OH abundances greater than 20% relative to H_2O. Since the methanol abundance for the objects studied here is on the order of a few percent, the contribution of alcohols to the 3.0 μm absorption can be neglected. Since the 3.0 μm band does not usually suffer from severe issues of blending and is strongest of the H_2O-ice absorption features, we use it to deduce the H_2O-ice column density as well as the ice "threshold" extinction.

Figure 4 shows the laboratory spectrum of 10 K H_2O-ice (Hudgins et al. 1993) overlaid on the optical depth spectra. Compared to the laboratory ice analog, the observed 3 μm ice profile has "excess" absorption longward of 3.05 μm and, in some cases, weak excess absorption at about 2.95 μm. Smith et al. (1993) noticed the latter feature in Taurus field stars on later spectral types and therefore attributed it to a photospheric or circumstellar feature. However, for the IC 5146 stars, the spectra with the most apparent excess at 2.96 μm are late G and early K giants, so a stellar origin is less likely. Also present in these spectra is "excess" absorption in the 3.2 to 3.6 μm region, known as the (enigmatic) "long-wavelength wing" (Baratta & Strazzulla 1990; Smith et al. 1993). Ammonia (NH_3) ice related species such as ammonium hydrates may account for some of this absorption as well as the excess at 2.96 μm (e.g., Chiar et al. 2000; Gibb et al. 2001). Some of the wing absorption may be accounted for by scattering in a model where spherical grains are coated with thick mantles or only the largest grains have mantles (Smith et al. 1993). Discrete features in the

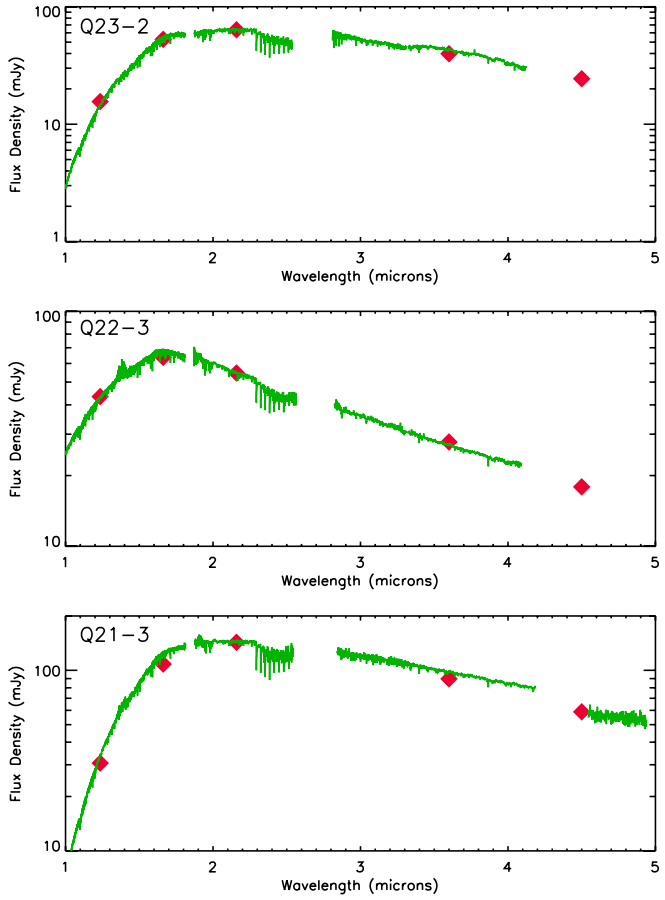

(b)

Figure 3. (Continued)

3.2 to 3.6 μm region contribute to the absorption: a feature at 3.47 μm is attributed to hydrocarbon-containing ices (Chiar et al. 1996; Brooke et al. 1996, 1999) and CH_3OH-ice exhibits a narrow absorption feature at 3.54 μm (Allamandola et al. 1992). However, in quiescent dense clouds the abundance of CH_3OH relative to H_2O-ice is less than 5%, so it does not contribute significantly (Chiar et al. 1996). Boogert et al. (2011) find the CH_3OH abundance to be ~7% for the isolated dense cores probed by background stars. Thus, much of the "wing" absorption remains a mystery.

Four of our sources have a detectable 3.47 μm feature. The optical depth, $\tau_{3.47}$, was calculated using a local third-degree polynomial to determine the continuum across the 3.2 to 3.8 μm region, avoiding the 3.30 to 3.33 μm region (where the telluric cancellation is poor) and the 3.4 to 3.6 μm region where the ice absorption is expected to be present. We determined $\tau_{3.47}$ using the average feature width ($\Delta\lambda = 0.105 \pm 0.004$ μm) and central wavelength ($\lambda_0 = 3.469 \pm 0.002$ μm) determined by Brooke et al. (1999). The results are given in Table 2. In addition, for Q21-1 and Q21-6, absorption in excess of the typical 3.47 μm feature is present. Figure 5 shows that this absorption is consistent with the CH_3OH amounts allowed by the observed 9.75 μm feature in the spectra of these same sources.

In spite of the excess wing absorption, the 3.0 μm absorption feature itself is well suited for calculating the H_2O-ice column density. We estimate the H_2O-ice column by scaling a Gaussian function with $\lambda_0 = 3.04$ μm with FWHM = 0.22 μm. On average, the column densities determined in this manner are about 10% larger than those determined using the 10 K H_2O-ice laboratory spectrum. The resulting column densities are listed in Table 3. The laboratory ice analog spectrum is also useful for assessing the contribution of pure H_2O-ice to the 6.0 and 13.0 μm spectral regions. In order to limit the contribution of ice to those spectral regions, we fitted the laboratory spectrum to the trough of the 3.0 μm absorption and calculated a residual across the entire *Spitzer* IRS spectrum. This calculated residual was then used to analyze the 9.7 μm silicate absorption profiles (Section 3.3) and the absorption features in the 5 to 8 μm region (Section 3.4).

3.1.1. H_2O-ice Threshold

The ice threshold is the A_V value below which ice absorption is not detected and therefore icy mantles are not present (Whittet 2003). The threshold A_V is generally higher for dense clouds that have active star formation and are forming intermediate- to high-mass stars, compared to quiescent clouds that form low-mass stars at a slow rate. Volatile ice species, like CO-ice, whose presence is more sensitive to local temperature and density conditions tend to have higher threshold extinction (Whittet et al. 1989; Chiar et al. 1995). The Taurus cloud, generally used as a model for the measurement of ice thresholds in pristine environments since it has the greatest number of ice absorption measurements toward background stars, exhibits a threshold of $A_V = 3.2 \pm 0.1$ mag (Whittet et al. 2001 and references therein). For the more active Serpens cloud, the H_2O-ice threshold is higher at $A_V \sim 6$ (Eiroa & Hodapp 1989), and for the ρ Ophiuchus cloud that is forming intermediate- to high-mass stars, the threshold is even higher at $A_V \sim 13$ mag (Tanaka et al. 1990).

For the IC 5146 cloud, we calculate the H_2O-ice threshold extinction by means of a linear least-squares fit including the uncertainties (error bars) in both A_V and $\tau_{3.0}$, resulting in a threshold of $A_V = 4.03 \pm 0.05$ mag (Figure 6). For consistency, we repeat the fit to the Whittet et al. (2001) data while taking the uncertainties in both A_V and $\tau_{3.0}$ into account, resulting in threshold extinction, $A_V = 3.19 \pm 0.07$. As demonstrated by the correlation lines in Figure 6, the slopes of the IC 5146 and Taurus correlation lines are similar: 0.072 ± 0.002 and 0.068 ± 0.003, respectively, suggesting that H_2O-ice-mantle growth with increasing extinction is similar in both clouds. This is in line with calculations that show that once the critical threshold A_V is reached—i.e., the first mono layer of ice is formed on the silicate or carbonaceous substrate—the local infrared radiation field has little effect on subsequent ice layer growth due to strong H-bonding between neighboring H_2O-ice molecules (Williams et al. 1992). The apparent increase of the threshold A_V in IC 5146 is likely to be an effect of foreground extinction given the distance of 950 pc to IC 5146 (Section 1). In fact, Neckel & Klare (1980) estimate the foreground extinction in the direction of IC 5146 to be ~0.8 mag, comparable to the difference in the threshold extinction between IC 5146 and Taurus.

3.2. CO and CO_2 Ice

Toward field stars behind dense clouds, the more volatile CO-ice ranges in abundance between 10% and 40% relative to H_2O-ice (Chiar et al. 1995; Whittet et al. 2009). We were able to acquire an *M*-band spectrum with IRTF-SpeX for one of the IC 5146 sources, Q21-1. Figure 7 shows the 4.67 μm CO ice absorption profile with the spectrum of the Taurus field star Elias 16 (Chiar et al. 1995) overlaid for comparison. Many of the sharp absorption peaks in the Q21-1 spectrum that dip below

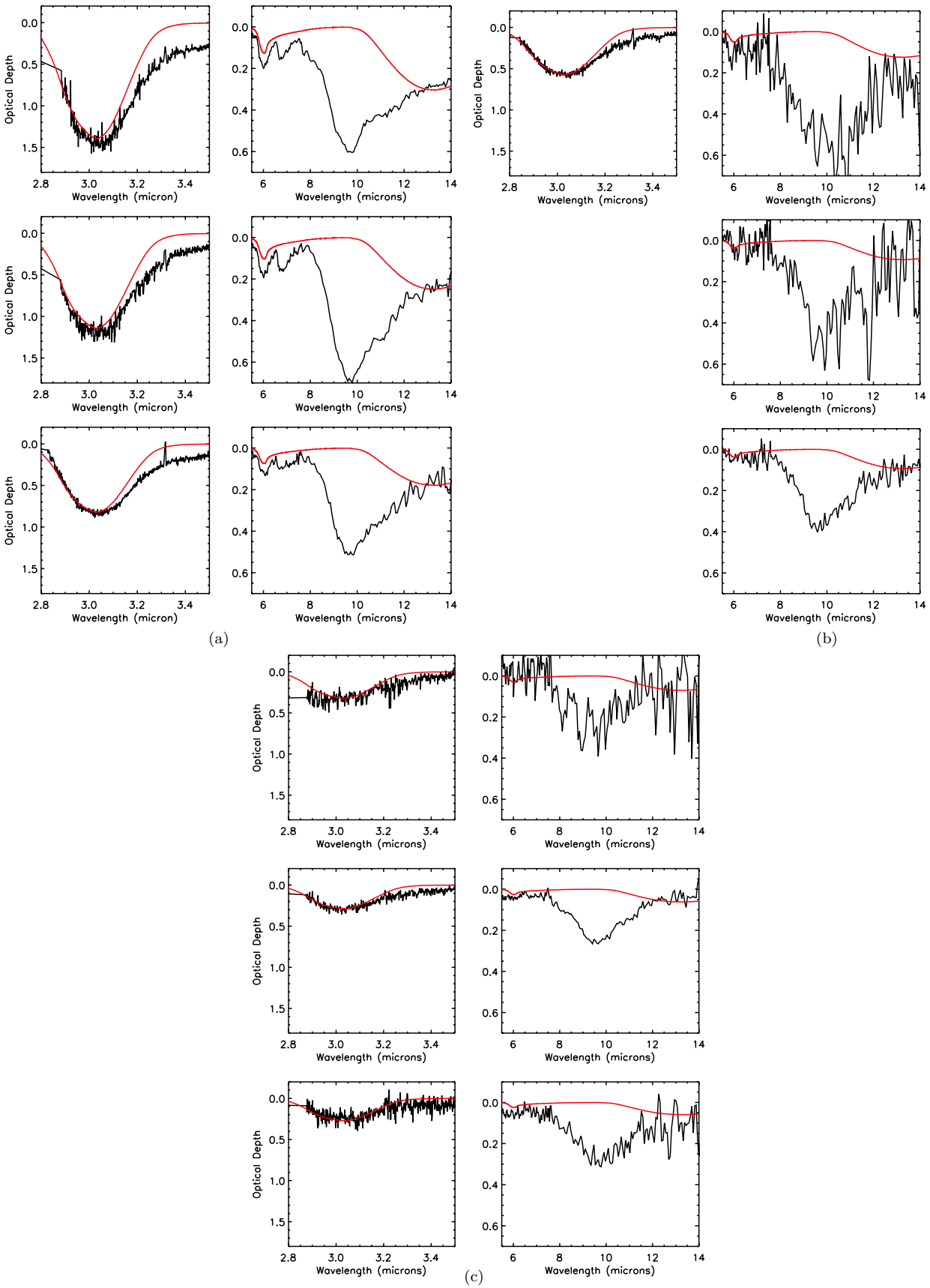

Figure 4. Optical depth profiles for the ice and dust features based on the reddened photosphere model matches as shown in the previous figure. Laboratory data (red lines) for H_2O ice at 10 K are overlaid on the observational data (black lines). (a) Profiles for (from top to bottom) Q21-1, Q21-6, and Q22-1. (b) Profiles for (from top to bottom) Q21-2, Q21-3, and Q23-2. (c) Profiles for (from top to bottom) Q21-4, Q21-5, and Q23-1.

(A color version of this figure is available in the online journal.)

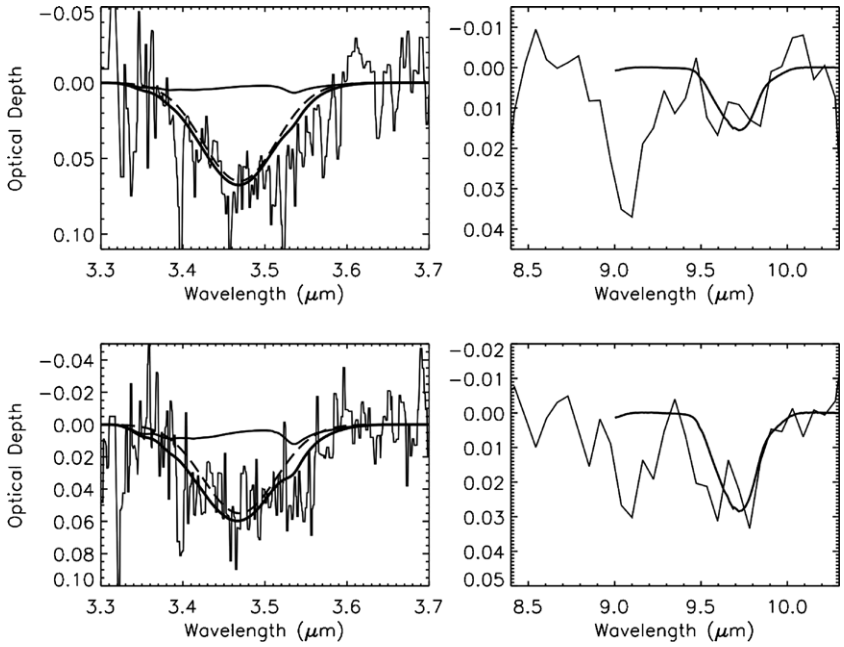

Figure 5. Absorption in the long-wavelength H_2O-ice wing (left panel) and 8.5–10 μm region after fitting local continua to remove H_2O-ice and silicate absorption (see Sections 3.1 and 3.5 for details) for Q21-1 (top) and Q21-6 (bottom). The left panel shows a Gaussian representing the average 3.47 μm feature profile as determined by Brooke et al. 1999 (dashed line), the weak CH_3OH ice feature (solid line) from laboratory data (Gerakines et al. 1995, 1996), and co-addition of those two features (the deepest smooth line). The contribution of CH_3OH at 3.54 μm is constrained by the strength of the maximum allowed CH_3OH feature detected at 9.75 μm (left panel; laboratory data shown as a smooth curve).

Table 2
Peak Optical Depths of Various Ice and Dust Components

Source ID	$\tau_{3.05}$	$\tau_{3.47}$	$\tau_{6.0}$	Comp. 1	Comp. 2	Comp. 3	Comp. 4	Comp. 5	$\tau_{9.7}$
Q21-1	1.45	0.065	0.19	0.04	0.04	0.07	0.06	0.00	0.602 ± 0.002
Q21-2	0.57	0.030	0.09:	0.10:	0.04:	0.07:	0.06	0.00	0.534 ± 0.110
Q21-3	...	...	0.04:	...	...	...	...	...	0.444 ± 0.026
Q21-4	0.31	<0.02	0.01:	...	...	...	...	...	0.281 ± 0.082
Q21-5	0.30	<0.01	0.04	0.02	0.02	0.02	0.02	0.00	0.259 ± 0.006
Q21-6	1.17	0.055	0.17	0.05	0.04	0.08	0.07	0.00	0.689 ± 0.008
Q22-1	0.82	0.048	0.11	0.03	0.04	0.04	0.04	0.00	0.509 ± 0.006
Q22-3	...	...	<0.01	...	...	...	...	...	<0.15
Q23-1	0.24	<0.04	0.06	0.03	0.03	0.03	0.03	0.00	0.297 ± 0.017
Q23-2	...	...	0.05	0.03	0.03	0.05	0.05	0.00	0.379 ± 0.026

Table 3
Column Densities of Various Ice and Dust Components

Source ID	$N(H_2O)$[a]	$N(CO)$	$N(NH_3)$	$N(CH_3OH)$
		$\times 10^{17}$ cm^{-2}		
Q21-1	25.2	6.83	0.6–1.1	0.24
Q21-2	9.84	...		
Q21-3	...	...		
Q21-4	5.18	...		
Q21-5	5.18	...		
Q21-6	20.0	...	0.4–0.8	0.32
Q22-1	14.2	...	0.3–0.7	0.16:[b]
Q22-3	...	...		
Q23-1	4.32	...		
Q23-2	...	...		

Notes.
[a] No SpeX data exist for Q21-3, Q22-3, and Q23-2.
[b] Colon denotes uncertain value.

the Elias 16 spectrum are due to (unresolved) gas-phase lines. Since the resolution is not high enough to model these lines, we use the relatively smooth Elias 16 spectrum to estimate the CO ice column density. The Elias 16 CO profile, and therefore also its column density, is scaled by a factor of 1.05 to give a CO ice column density for Q21-1 equal to 6.83×10^{17} cm^{-2} (Table 3). This results in CO/H_2O column density ratio equal to 0.27, in the same range found for other dense cloud lines of sight.

The bending mode of CO_2 occurs at 15.3 μm and is contained in the IRS short-high spectrum for Q21-1 previously presented by Whittet et al. (2009). They found that the profile shape of the 15.3 μm CO_2 feature is unvarying in the dark clouds sampled (Taurus, IC 5146, Serpens) despite some scatter in the abundance relative to H_2O-ice which may be due to differences in how the elemental oxygen is distributed in the main oxygen-containing ice species (H_2O, CO, CO_2). They find that the CO_2 abundance relative to H_2O is ~0.2 for Taurus and ~0.3 for IC 5146 (Q21-1).

3.3. Silicates

Differences in the profile shape of the interstellar silicate feature observed in dense clouds and the diffuse interstellar medium (ISM) have been noted previously. Generally, emissivity curves based on observations of the M supergiant μ Cephei (Russell et al. 1975) and Orion's Trapezium region (Forrest et al. 1975) are used to fit the observed absorption features in the diffuse ISM and dense clouds, respectively (e.g., Roche

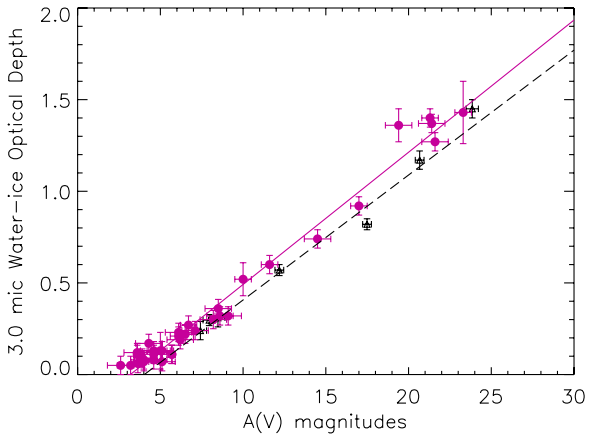

Figure 6. Optical depth of the 3.0 μm H_2O-ice feature vs. visual extinction for field stars behind the IC 5146 (this work, black symbols) and Taurus (Whittet et al. 2001, purple symbols) dark clouds. A_V values for the IC 5146 background stars are based on $E(J-K)$ as determined from the reddened photospheric model fit and an appropriate extinction law (see Sections 2.1 and 2.2). Determination of A_V for Taurus sources is discussed in detail in Whittet et al. (2001). A weighted least-squares fit to the IC 5146 data (dashed black line) and Taurus (purple line) taking uncertainties in $\tau_{3.0}$ and A_V into account results in threshold extinctions of $A_V = 4.02$ mag and $A_V = 3.19$ mag, respectively. Accounting for the foreground extinction toward IC 5146 ($\sim$0.8 mag) brings the threshold A_V for IC 5146 and Taurus into agreement.

(A color version of this figure is available in the online journal.)

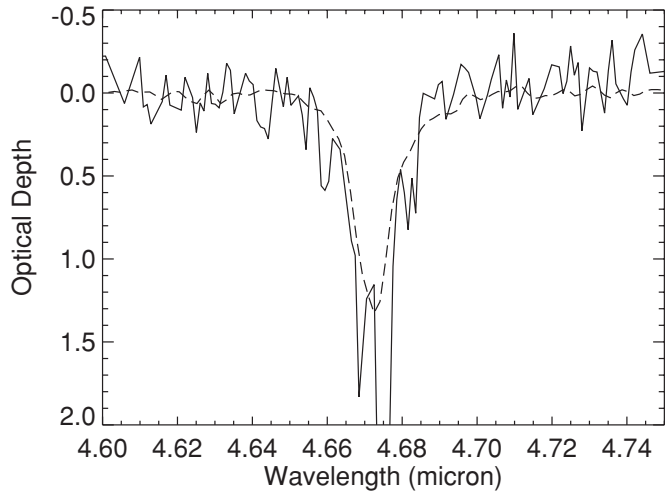

Figure 7. Optical depth spectrum in the region of the CO ice absorption feature for Q 21-1 (solid line). The (scaled) profile for the Taurus field star, Elias 16 is also shown for comparison (dashed line). See the text for details.

& Aitken 1984; Whittet et al. 1988; Bowey et al. 1998). The Trapezium silicate profile peaks at 9.6 μm compared to 9.9 μm for the μ Cephei profile. Furthermore, van Breemen et al. (2011) find that the "dense cloud" silicate profiles differ substantially from the diffuse ISM profiles peaking at shorter wavelengths relative to the diffuse ISM profiles. To illustrate the robustness of these differences, we compare the IC 5146 field star profiles with the highest signal-to-noise ratio (S/N) to that of the diffuse ISM toward the Wolf–Rayet star, WR 98a (from Chiar & Tielens 2006), in Figure 8. All profiles have been normalized to unity at 10.1 μm. The normalization wavelength was chosen to avoid regions that could be contaminated by photospheric or ice absorption. This comparison shows that there are small differences in the dense cloud spectra on the blue side; these differences may be due to residual photospheric absorption (like SiO) that is not fully accounted for in the models. In addition,

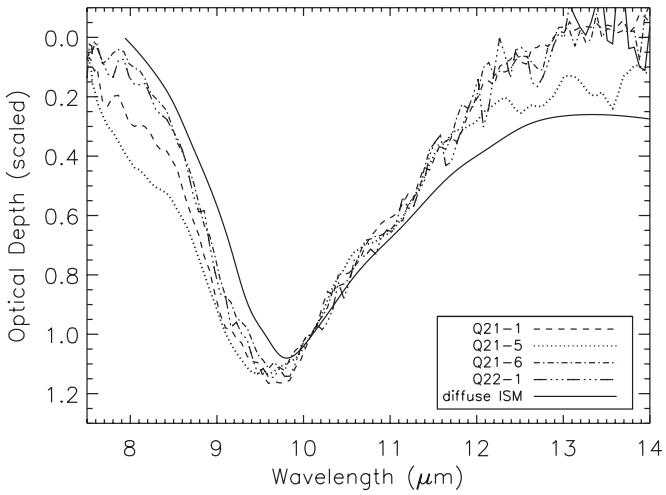

Figure 8. Comparison of the silicate profiles for the highest extinction sources Q21-1, Q-21-6, Q22-1 (dashed lines), the low-extinction source Q21-5 (dotted line), and the diffuse ISM as probed by WR 98a (solid line; Chiar et al. 1996). The spectra are normalized at 10.1 μm. Small differences are noticeable on the blue wing of the feature; these may be due to photospheric absorption in the field stars. For the high-extinction sources, moderate excess absorption at the bottom of the feature ($\sim$9.8 μm) is due to CH_3OH-ice absorption (see Figure 12).

there is "excess" absorption in the trough of the feature in the highly reddened sources due to CH_3OH- and NH_3-ice absorption (see Section 3.5). Otherwise, the silicate profiles show little difference in the less and more reddened lines of sight in this small sample. All the IC 5146 field star profiles are shifted blueward compared to the diffuse ISM profile.

3.4. Absorption Features in the 5–8 μm Region

Absorption features centered around 6.0 and 6.8 μm are detected in six out of ten lines of sight in IC 5146 (see Table 2). These features have been previously detected in the spectra of high-mass (Schutte et al. 1996; Keane et al. 2001) and low-mass YSOs (Boogert et al. 2008), dense clouds as probed by a few field stars (Knez et al. 2005), and dense cores as probed by field stars (Boogert et al. 2011).

It has been shown previously that the absorption feature at 6.0 μm cannot be fully accounted for by H_2O-ice (e.g., Tielens et al. 1984; Keane et al. 2001; d'Hendecourt et al. 1996). In fact, if the 6.0 μm absorption were fitted with H_2O-ice, the O–H stretching mode at 3.0 μm is overestimated by up to a factor of three for high-mass YSOs (Schutte et al. 1996; Gibb et al. 2000; Keane et al. 2001). While CH_3OH also has a strong band at 3.07 μm (e.g., Hudgins et al. 1993) which can skew the apparent 3.0/6.0 ratio, this is unlikely to be a problem in quiescent lines of sight since the CH_3OH abundance, determined by analysis of absorption at 3.54 and 9.7 μm, is less than 5% of the H_2O-ice (see Section 3.5 and also Chiar et al. 1996). Other proposed contributors to the absorption at 6.0 μm are formic acid (HCOOH), formaldehyde (H_2CO), and the C–C stretch in aromatics. Combining our small field star sample with the larger sample by Boogert et al. (2008; 41 low-mass YSOs, eight high-mass YSOs, and two field stars),[13] we examine the relationship between the 3.0 μm H_2O-ice and the 6.0 μm absorption bands. Figure 9 shows graphically that the observed 6 μm absorption cannot be fully accounted for by 10 K H_2O-ice. The

[13] For sources with extremely deep 3.0 μm bands ($\tau_{3.0} > 5$), where the depths cannot be measured due to lack of detectable flux, Boogert et al. (2008) estimate $\tau_{3.0}$ using the H_2O libration mode at 13 μm. This is the cause of the larger error bars on those data points.

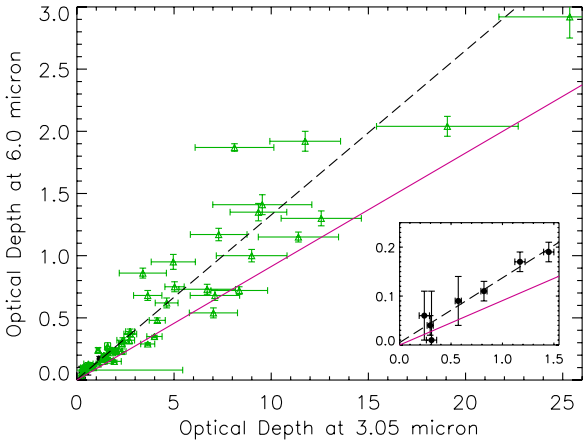

Figure 9. Relationship between the optical depths of the 3.05 and 6.0 μm features. Data points are shown for the observed features in IC 5146 (black points) and low-mass YSOs (green points; Boogert et al. 2008). The IC 5146 points are clustered in the lower left corner of the plot; the inset shows this region in more detail. The purple line is the ratio, $\tau_{6.0}/\tau_{3.05}$, for laboratory H_2O-ice at 10K (Hudgins et al. 1993). The black dashed line is the least-squares fit to just the IC 5146 sources.

(A color version of this figure is available in the online journal.)

shallower line shows the $\tau_{6.0}/\tau_{3.05}$ ratio for the 10 K laboratory H_2O-ice analog from Hudgins et al. (1993). The steeper line is the correlation line for the IC 5146 field stars. Significantly, nearly all of the data points, including those of the field stars where little to no (energetic or thermal) processing of the ices is expected, lie above the laboratory ice line. At larger values of $\tau_{3.05}$ (which roughly scales with A_V), the scatter between the data points increases, indicative of increased alteration of the ices in the most heavily obscured YSOs.

Boogert et al. (2008) recently decomposed the 6.0 and 6.85 μm features into five components in addition to a contribution from H_2O-ice using spectra from a large sample of low-mass and high-mass YSOs. They decompose the 6.0 μm band into two components referred to as C1 ($\lambda = 5.84\,\mu$m) and C2 ($\lambda = 6.18\,\mu$m). The C1 component is explained mostly by solid HCOOH and H_2CO with abundances up to 6% relative to H_2O (Boogert et al. 2008). The C2 component is also due to a blend of several species, with NH_3 being the most dominant. Monomers, dimers, and small multimers of H_2O mixed with CO_2 as well as contributions from salts are also possible (Boogert et al. 2008). The 6.85 μm absorption band shows great variation from source to source for the high-mass and low-mass YSOs that have been studied (Keane et al. 2001; Boogert et al. 2008). This band is also decomposed into a short-wavelength (C3, $\lambda = 6.755\,\mu$m) and long-wavelength (C4, $\lambda = 6.943\,\mu$m) component by Boogert et al. (2008). Both components are attributed to the ammonium ion, which would have to be produced by low-temperature reactions since both components are also detected in quiescent cloud spectra. Underlying the C1 through C4 components is a fifth broad component (C5) whose origin may be related to processing of ices in the vicinity of the embedded YSOs (Boogert et al. 2008).

We use the component definitions as determined by Boogert et al. (2008) to investigate their presence in the field star spectra. We show the component decomposition for the four sources with the highest S/N in Figure 10. To be consistent with the determination of the C1 through C5 components in the studies by Boogert et al. (2008, 2011), we fit a local continuum across the 5 to 8 μm region. The shape of the 5 to 8 μm region (where the absorption bands of photospheric H_2O and SiO appear) of the

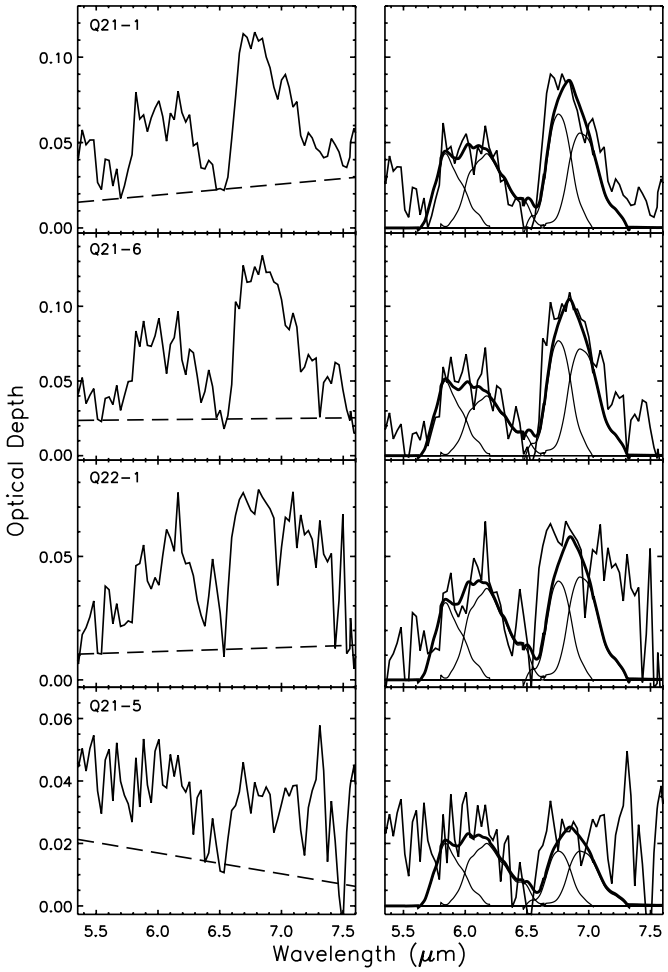

Figure 10. Residual absorption in the 5.4–7.6 μm region after subtraction of pure H_2O-ice. Left: a local straight-line continuum (dashed line) is fitted across this spectral region (see the text for details). Right: continuum-subtracted spectra. Thin lines represent components C1, C2, C3, and C4 as described in the text. The C5 component is not present in these sources. Thick lines represent the sum of the four components.

observed spectra is not always well fitted by the computational models, so a straight-line continuum is fitted across this region. This local continuum, fitted using points around 5.5, 6.5, and/or 7.5 μm, removes the apparent offset of the optical depth spectra (see the left panels in Figure 10). Following the subtraction of the local continuum, we decompose the 6.0 and 6.8 μm features in their components (see the right panels in Figure 10). The C5 component is not apparent in any of our spectra, in line with the suggestion that this component is due to the presence of processed ices in the vicinity of embedded objects (Boogert et al. 2008). We investigate the correlation of the C1 through C4 components with the H_2O-ice column density. Along with the C1 through C4 measurements for the IC 5146 field stars in this paper, we also include the two field stars (Elias 16, EC118) and the YSOs from Boogert et al. (2008). For consistency with the Boogert et al. (2008, 2011) studies, we normalize the component depth (e.g., τ_{C1}) to $N(H_2O)$ and plot that against $N(H_2O)$ to trace the component growth relative to the ice column (Figure 11). The field stars (solid circles) seem to follow the trends previously noted for the YSOs. We find that C2 shows a tight relationship of decreasing strength with increasing $N(H_2O)$ suggesting that this component is less volatile than H_2O-ice itself. C1 and C4 show more scatter. It is interesting to note

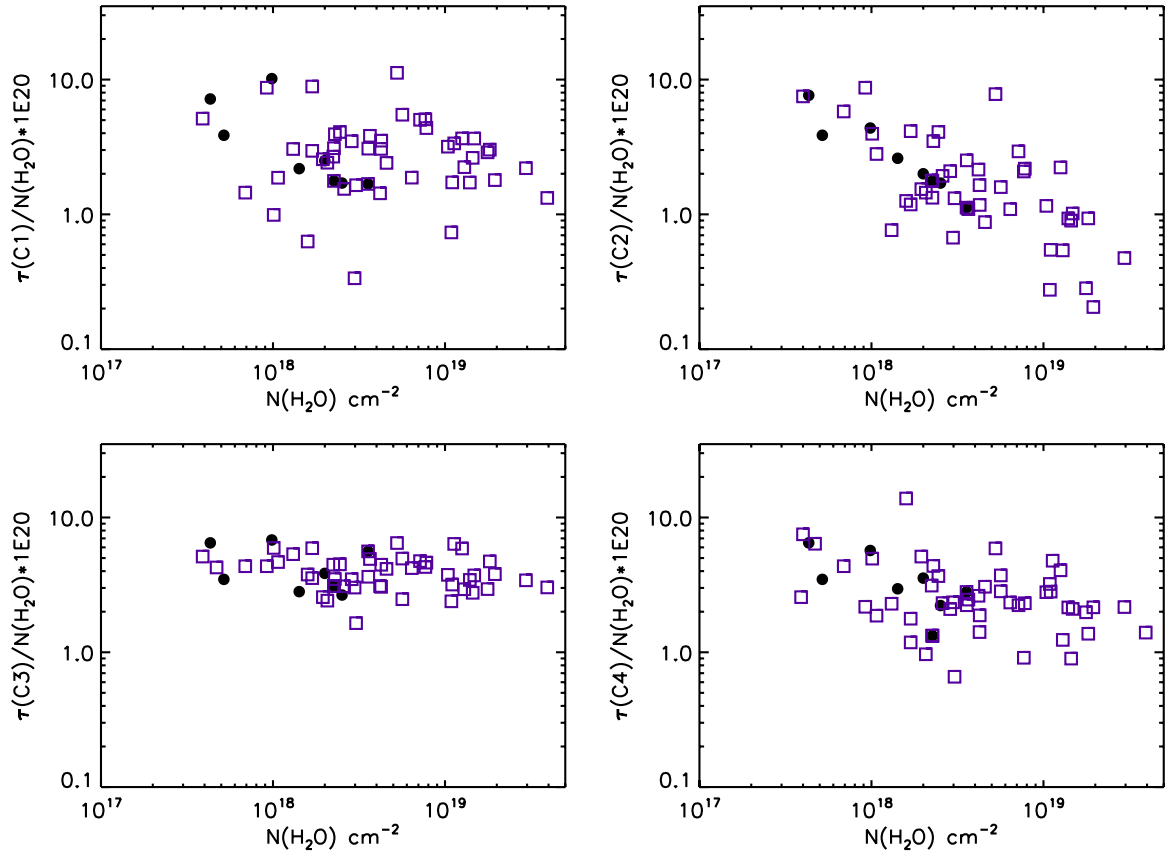

Figure 11. Correlation of the C1, C2, C3, and C4 absorption components with H_2O-ice column density. The optical depths of the C1 through C4 components are normalized to $N(H_2O)$. Purple squares are the YSO data from Boogert et al. (2008) and solid circles are data for field stars from IC 5146 (this work), Elias 16 (Taurus; Boogert et al. 2008), and EC118 (Serpens; Boogert et al. 2008).

(A color version of this figure is available in the online journal.)

that the C1 and C2 components seem to be of equal depth in each field star spectrum; this does not appear to be the case for the YSO spectra studied by Boogert et al. (2008) and is perhaps indicative of the sensitivity of one or both of these components to the UV or temperature processing that takes place in the environment around YSOs. The (normalized) C3 component shows a flat relationship with $N(H_2O)$, linking it as a non-volatile ice component that is not sensitive to varying temperature or energetic conditions of YSO environments.

3.5. Weak Ice Features in the 8.5 to 10 μm Region

The 8.5 to 10 μm region contains the N–H vibration inversion mode of NH_3 (d'Hendecourt & Allamandola 1986), the C–O stretching vibration of CH_3OH (Sandford & Allamandola 1993) as well as the O–O symmetric and asymmetric stretching mode of O_3 (Bennett & Kaiser 2005). Substructure at these wavelengths appears at the bottom of the silicate feature for the most highly extincted sources, Q21-1, Q21-6, and possibly Q22-1. We also examine the high S/N spectrum of Q21-5. For this source, which has relatively lower extinction (see Table 1), we do not expect to see the weak ice absorptions in the 8.5 to 10 μm region. So, we use this source as a check that the substructure detected in the high-extinction sources is not due to an artifact in the data reduction process. For all four sources, we fitted and subtracted a local polynomial continuum in the 8.4 to 10.5 μm region of the optical depth spectra in order to subtract the contribution of the broad silicate absorption. The continuum fits and resulting residuals are compared in Figure 12 in the left and right panels, respectively. In the spectra of Q21-1, Q21-6, and Q22-1, an absorption feature appears at 9.0 μm with FWHM of about 24 cm^{-1}. A second absorption feature at 9.7 μm, with FWHM of $\sim$38 cm^{-1}, is also present (tentatively in Q 22-1). We discuss the likely identifications of these features below.

We attribute the weak absorption at $\sim$9.7 μm, present in the spectra of Q 21-1 and Q 21-6 (and tentatively Q22-1), to the C–O stretching vibration in CH_3OH-ice, that occurs at about 9.75 μm (Sandford & Allamandola 1993). As shown in Figure 5, the CH_3OH identification is supported by residual absorption in the long-wavelength wing of the 3 μm H_2O-ice feature that is not accounted for by the typical 3.47 μm "hydrocarbon ice" feature. Assuming an FWHM equal to 29 cm^{-1} and intrinsic strength of $A = 1.8 \times 10^{-17}$ cm molecule^{-1} (d'Hendecourt & Allamandola 1986), we calculate the column density of CH_3OH for the three lines of sight (Table 3). The CH_3OH/H_2O ratio is in the range of 1%–2% for these sources. This is well within the previous limiting value (<5%) determined for the Taurus dark cloud (Chiar et al. 1996).

The N–H inversion mode occurs near 9.1 μm, and its central wavelength is highly sensitive to matrix neighbors. Embedded in a polar matrix, the feature peaks at 8.97 μm, and in an apolar matrix, the feature peaks at 9.57 μm (Lacy et al. 1998). The observed 9.0 μm feature falls in the range of the N–H umbrella mode, although it is narrower than the available NH_3 ice analogs which have widths equal to $\sim$50 cm^{-1} (d'Hendecourt & Allamandola 1986; Lacy et al. 1998). Given the difficulty in

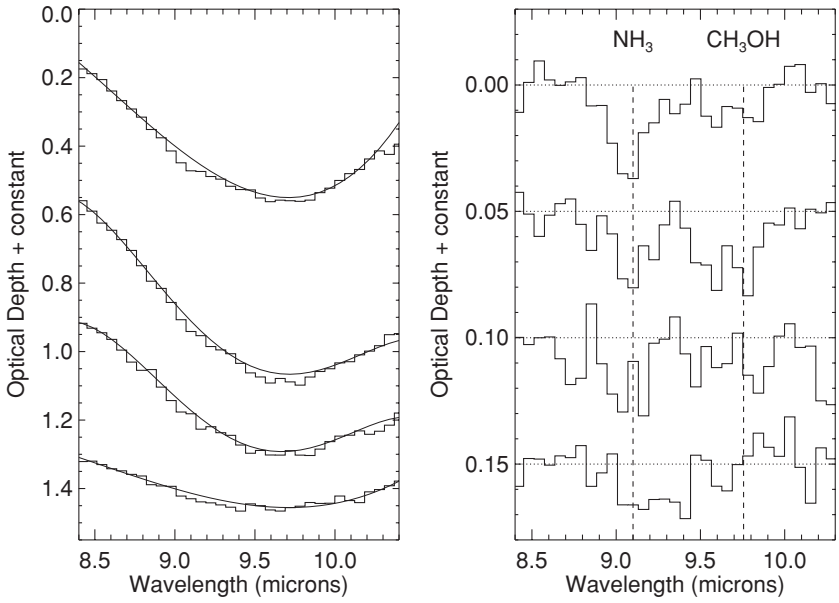

Figure 12. Left: silicate profiles for the sources (from top to bottom) Q21-1, Q21-6, Q22-1, and Q21-5. Light line is the local polynomial continuum used to subtract off the silicate absorption to extract the weak ice features. Right: continuum-subtracted optical depth spectra in the region of the silicate absorption. Sources are the same as in the left panel. The approximate wavelength positions of NH_3 and CH_3OH are shown. Note that the peak wavelength of NH_3 is extremely sensitive to temperature and neighboring molecules in the ice.

extracting the ice feature from the bottom of the broad silicate absorption, it is possible that we have underestimated the width by a factor of two. Taking this uncertainty into account and using an intrinsic strength of $A = 1.7 \times 10^{-17}$ cm molecule^{-1} for the ν_2 umbrella mode of NH_3 (d'Hendecourt & Allamandola 1986), we compute column densities for Q 21-1, Q 21-6, and Q 22-1. These are given in Table 3. For all three sources, the column of NH_3 relative to H_2O-ice ranges from 2% to 5%.

Ozone (O_3) ice has absorption features at 9.06 μm and 9.64 μm due to the O–O symmetric and asymmetric stretch (Bennett & Kaiser 2005). The O–O asymmetric stretch is ~80 times stronger than that of the corresponding symmetric stretch (Bennett & Kaiser 2005). Given the depth of the observed absorption centered at 9.7 μm, O_3-ice would contribute a negligible amount to the optical depth at 9.0 μm. Thus, it is unlikely that O_3 contributes significantly to the ices in these lines of sight.

4. EXTINCTION

In the diffuse ISM, the extinction due to silicates (i.e., $\tau_{9.7}$) shows a tight linear correlation with A_V (Whittet 2003 and references therein). Whittet et al. (1988) and Chiar et al. (2007) showed that, in dense clouds, the optical depth of the 9.7 μm silicate feature ($\tau_{\rm silicate}$) is weaker per unit A_V compared to the diffuse ISM. The Chiar et al. (2007) study analyzed 30 spectra toward six different dense clouds, including IC 5146. For that sample, $\tau_{9.7}$ was computed using a low-order polynomial fitted over the 5 to 15 μm region and an estimate of $E(J-K)$ based on a likely range of spectral types for the background stars. The $\tau_{9.7}$ and $E(J-K)$ estimates thus vary slightly from the more thorough analysis presented here; most values are within 20% of those determined previously. A recent reanalysis of the Chiar et al. (2007) sample reports that the *total* optical depth at 9.7 μm ($\tau_{9.7}$) correlates with the extinction in the K band, A_K (McClure 2009), and the data points lie along the same correlation line as for the diffuse ISM. However, there are some caveats to this illusory agreement in correlations. First, the total τ at 9.7 μm includes the underlying "continuum" extinction, the extinction due to the silicates themselves, and a small contribution from ices (for the high-extinction sources) so a correlation between $\tau_{9.7}$ and A_K does not speak directly to the relation between the silicate and K-band extinction. Second, for the diffuse ISM studies, the optical depth due to the silicates alone (i.e., $\tau_{\rm silicate}$) is shown to correlate with the visual extinction (Roche & Aitken 1984; Rieke & Lebofsky 1985; Bowey et al. 2004; Chiar & Tielens 2006). In the diffuse ISM studies, continuum extinction due to the ISM dust and the dust shells of the Wolf–Rayet stars is accounted for by a power-law extinction curve or $1/\lambda$ emissivity curve, respectively.

We illustrate the relationship between the extinction quantities in Figure 13. Optical depth is related to the extinction by $\tau_\lambda = -\ln(10^{-A_\lambda/2.5})$. The upper frame in Figure 13 plots $\tau_{9.7}$, the peak silicate optical depth excluding the continuum extinction versus the $E(J-K)$ color excess for the IC 5146 sources and diffuse ISM sources (from Whittet 2003 and references therein). As discussed previously by Chiar et al. (2007), the diffuse ISM sources follow a tighter and steeper correlation compared to the IC 5146 sources. In the lower panel of Figure 13, we follow McClure's method and plot the *total* optical depth at 9.7 μm (including continuum and silicate extinction) for the IC 5146 sources and the diffuse ISM sources. The continuum extinction at 9.7 μm is calculated using the Indebetouw et al. (2005) extinction law ($A_\lambda/A_K = 0.43$ at 8 μm), assuming $A_{9.7} = A_8$, where A_K is determined from the continuum fits shown in Figure 1. The correlation lines are least-square fits to the data and show that including continuum extinction shifts both the diffuse ISM and dense cloud points up in the $\tau_{9.7}$ versus $E(J-K)$ plot.

5. SUMMARY AND DISCUSSION

Most comparisons of the relative abundances, temperature, and evolution of ices in star formation regions are made with respect to the Taurus dark cloud which is used throughout the literature as the prototypical pristine environment for the

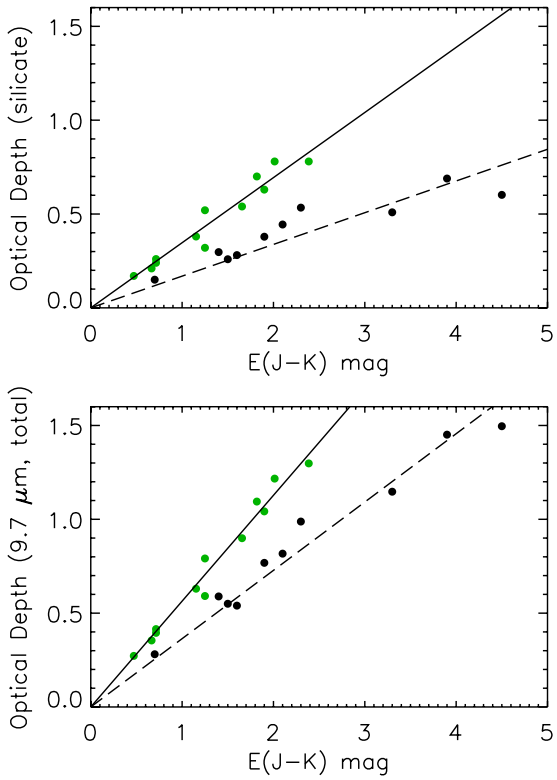

Figure 13. Top: the optical depth of the silicate feature at 9.7 μm vs. the $E(J-K)$ color excess. Bottom: the total optical depth at 9.7 μm (including continuum extinction) vs. $E(J-K)$. Green points are for the diffuse ISM (Whittet 2003 and references therein). In the bottom frames, the diffuse ISM τ values (green circles) do not include continuum extinction (see the text for details).

(A color version of this figure is available in the online journal.)

study of dust and ices. This is because the fortuitous placement of bright field giants behind the Taurus cloud have made spectroscopic studies practical. In this paper, we present a spectroscopic study of the quiescent IC 5146 dark cloud which was made possible by the sensitive IRS instrument on *Spitzer* and the SpeX instrument on the IRTF. We have shown that the quiescent IC 5146 dark cloud shares many of the characteristics of the Taurus cloud; we summarize our results here.

IRTF-SpeX 2 μm spectra were used to classify the IC 5146 background stars with stunning accuracy, thereby allowing continua to be fitted over the full 2 to 20 μm range, resulting in reliable determinations of the extinction, ice, and silicate absorption profiles. We show that, after taking foreground extinction into account, the H_2O-ice extinction threshold in the IC 5146 dark cloud is nearly equivalent to that in Taurus, showing the universality of the onset of ice-mantle growth in regions far from internal sources of radiation. The growth of the icy mantles as measured by the increase of $\tau_{3.0}$ with respect to A_V is similar in both clouds as shown by the comparable slopes of the regression lines on a $\tau_{3.0}$–A_V plot.

We have compared ice abundances in the IC 5146 cloud to Taurus and low- and high-mass YSOs (Table 4). Previous estimates of the abundances of CH_3OH and NH_3 in dense clouds were based on limits only (Chiar et al. 1996; Gibb et al. 2001). However, recent laboratory (Bottinelli et al. 2010) and computational simulations (Cuppen et al. 2009) suggest that the hydrogenation process that forms CH_3OH should be efficient in cold environments. The recent observational study by Boogert et al. (2011) of ices in isolated dense cores finds

Table 4
Relative Ice Abundances in Different Environments

Ice	IC 5146	Taurus	Low-mass YSOs	High-mass YSOs
H_2O	1	1	1	1
CO	0.27	0.32 ± 0.12	0.32	0.12 ± 0.07
CO_2	0.35	0.19	0.19 ± 0.13	0.18 ± 0.07
CH_3OH	~0.02	<0.05	0.08	<0.04–0.32
NH_3	~0.05	<0.10	<0.27	<0.02–0.17
OCN^-	<0.01	<0.01	<0.002–0.057	<0.002–0.063

CH_3OH abundances in the 5% to 12% range, in line with the idea of efficient production of CH_3OH in the coldest environments. Here we have shown that CH_3OH and NH_3 are present in the quiescent cloud medium at the 2% to 5% level relative to H_2O-ice. In general, CH_3OH ice is more abundant in YSO environments compared to quiescent dark clouds. The NH_3 abundances for the dense cloud and YSO environments show wide variation, perhaps reflecting the difficulty of the spectroscopic measurement rather than the sensitivity of NH_3-ice itself to cloud conditions. In either case, NH_3-ice is an important mantle constituent in all dense cloud environments and therefore an important reservoir of elemental N in these regions. The CO-ice abundance appears to be similar in the IC 5146 and Taurus clouds, while the CO_2 abundance is elevated in IC 5146 compared to Taurus. Whittet et al. (2009) attribute this difference to variations in gas-phase chemistry, but point out that the amount of oxygen depleted into the ices is consistent in the two clouds. As has been previously noted (Kerr et al. 1993; Thi et al. 2006), the YSOs show a large variation in CO abundance, reflecting the sensitivity of CO to the environmental conditions (temperature, UV), while the CO_2 abundance is remarkably consistent (with the exception of the IC 5146 measurement).

Finally, our results firmly support the conclusions by Chiar et al. (2007) that the silicate optical depth, $\tau_{9.7}$, grows more slowly per unit A_V in dense clouds relative to the diffuse ISM. The change in dust characteristics that cause the difference in the $\tau_{9.7}$–A_V relation is still an open question.

This work is based (in part) on observations made with the *Spitzer Space Telescope*, which is operated by the Jet Propulsion Laboratory, California Institute of Technology under a contract with NASA. Support for this work was provided to J.E.C. by NASA through an award issued by JPL/Caltech and to Y.J.P., L.J.A., K.E., T.P.G., T.L.R., and S.A.S. by NASA. L.J.A. gratefully acknowledges support from NASA's Astrobiology (grant 811073.02.12.03) and Laboratory Astrophysics (grant 09-APRA09-0019) programs. D.C.B.W. is grateful to the NASA Exobiology and Evolutionary Biology Program (grant NNX07AK38G) and the NASA Astrobiology Institute (grant NNA09DA80A) for financial support. R.E.M. and T.R.G. are supported by the Gemini Observatory, which is operated by the Association of Universities for Research in Astronomy, Inc., on behalf of the international Gemini partnership of Argentina, Australia, Brazil, Canada, Chile, the United Kingdom, and the United States of America. The work is also based in part on observations made at the Infrared Telescope Facility, which is operated by the University of Hawaii under Cooperative Agreement no. NCC 5-538 with the National Aeronautics and Space Administration, Science Mission Directorate, and Planetary Astronomy Program. This publication makes use of data products from the Two Micron All Sky Survey, which is a joint project

of the University of Massachusetts and the Infrared Processing and Analysis Center/California Institute of Technology, funded by the National Aeronautics and Space Administration and the National Science Foundation.

Facilities: Spitzer(IRS), *IRTF*(SpeX)

REFERENCES

Allamandola, L. J., Sandford, S. A., Tielens, A. G. G. M., & Herbst, T. M. 1992, ApJ, 399, 134
Baratta, G. A., & Strazzulla, G. 1990, A&A, 240, 429
Bennett, C. J., & Kaiser, R. I. 2005, ApJ, 635, 1362
Bergin, E. A., Melnick, G. J., Gerakines, P. A., Neufeld, D. A., & Whittet, D. C. B. 2005, ApJ, 627, L33
Bessell, M. S., & Brett, J. M. 1988, PASP, 100, 1134
Boogert, A. C. A., et al. 2008, ApJ, 678, 985
Boogert, A. C. A., et al. 2011, ApJ, 729, 92
Bottinelli, S., et al. 2010, ApJ, 718, 1100
Bowey, J. E., Adamson, A. J., & Whittet, D. C. B. 1998, MNRAS, 298, 131
Bowey, J. E., Rawlings, M. G., & Adamson, A. J. 2004, MNRAS, 348, L13
Brooke, T. Y., Sellgren, K., & Geballe, T. R. 1999, ApJ, 517, 883
Brooke, T. Y., Sellgren, K., & Smith, R. G. 1996, ApJ, 459, 209
Cambrésy, L. 1999, A&A, 345, 965
Campins, H., et al. 2010, Nature, 464, 1320
Chiar, J. E., Adamson, A. J., Kerr, T. H., & Whittet, D. C. B. 1994, ApJ, 426, 240
Chiar, J. E., Adamson, A. J., Kerr, T. H., & Whittet, D. C. B. 1995, ApJ, 455, 234
Chiar, J. E., Adamson, A. J., & Whittet, D. C. B. 1996, ApJ, 472, 665
Chiar, J. E., & Tielens, A. G. G. M. 2006, ApJ, 637, 774
Chiar, J. E., Tielens, A. G. G. M., Whittet, D. C. B., Schutte, W. A., Boogert, A. C. A., Lutz, D., van Dishoeck, E. F., & Bernstein, M. P. 2000, ApJ, 537, 749
Chiar, J. E., et al. 2007, ApJ, 666, L73
Cohen, M., Wheaton, W. A., & Megeath, S. T. 2003, AJ, 126, 1090
Cuppen, H. M., van Dishoeck, E. F., Herbst, E., & Tielens, A. G. G. M. 2009, A&A, 508, 275
Cushing, M. C., Rayner, J. T., & Vacca, W. D. 2005, ApJ, 623, 1115
Cushing, M. C., Vacca, W. D., & Rayner, J. T. 2004, PASP, 116, 362
Decin, L., & Eriksson, K. 2007, A&A, 472, 1041
d'Hendecourt, L. B., & Allamandola, L. J. 1986, A&AS, 64, 453
d'Hendecourt, L., et al. 1996, A&A, 315, L365
Dobashi, K., Yonekura, Y., Mizuno, A., & Fukui, Y. 1992, AJ, 104, 1525
Eiroa, C., & Hodapp, K. 1989, A&A, 210, 345
Elias, J. H. 1978, ApJ, 223, 859
Forrest, W. J., Gillett, F. C., & Stein, W. A. 1975, ApJ, 195, 423
Gerakines, P. A., Schutte, W. A., & Ehrenfreund, P. 1996, A&A, 312, 289
Gerakines, P. A., Schutte, W. A., Greenberg, J. M., & van Dishoeck, E. F. 1995, A&A, 296, 810
Gibb, E. L., Whittet, D. C. B., Boogert, A. C. A., & Tielens, A. G. G. M. 2004, ApJS, 151, 35
Gibb, E. L., Whittet, D. C. B., & Chiar, J. E. 2001, ApJ, 558, 702
Gibb, E. L., et al. 2000, ApJ, 536, 347
Harvey, P. M., et al. 2008, ApJ, 680, 495
Heras, A. M., et al. 2002, A&A, 394, 539
Houck, J. R., et al. 2004, ApJS, 154, 18
Hudgins, D. M., Sandford, S. A., Allamandola, L. J., & Tielens, A. G. G. M. 1993, ApJS, 86, 713
Indebetouw, R., et al. 2005, ApJ, 619, 931
Keane, J. V., Tielens, A. G. G. M., Boogert, A. C. A., Schutte, W. A., & Whittet, D. C. B. 2001, A&A, 376, 254
Kerr, T. H., Adamson, A. J., & Whittet, D. C. B. 1993, MNRAS, 262, 1047
Knez, C., et al. 2005, ApJ, 635, L145
Lacy, J. H., Faraji, H., Sandford, S. A., & Allamandola, L. J. 1998, ApJ, 501, L105
Lada, C. J., Alves, J., & Lada, E. A. 1999, ApJ, 512, 250
McClure, M. 2009, ApJ, 693, L81
Mottl, M., Glazer, B., Kaiser, R., & Meech, K. 2007, Chem. Erde/Geochemistry, 67, 253
Neckel, T., & Klare, G. 1980, A&AS, 42, 251
Rayner, J. T., Cushing, M. C., & Vacca, W. D. 2009, ApJS, 185, 289
Rayner, J. T., Toomey, D. W., Onaka, P. M., Denault, A. J., Stahlberger, W. E., Vacca, W. D., Cushing, M. C., & Wang, S. 2003, PASP, 115, 362
Reach, W. T., et al. 2005, PASP, 117, 978
Rieke, G. H., & Lebofsky, M. J. 1985, ApJ, 288, 618
Rivkin, A. S., & Emery, J. P. 2010, Nature, 464, 1322
Roche, P. F., & Aitken, D. K. 1984, MNRAS, 208, 481
Russell, R. W., Soifer, B. T., & Forrest, W. J. 1975, ApJ, 198, L41
Sandford, S. A., & Allamandola, L. J. 1993, ApJ, 417, 815
Schulz, R., Owens, A., Rodriguez-Pascual, P. M., Lumb, D., Erd, C., & Stüwe, J. A. 2006, A&A, 448, L53
Schutte, W. A., et al. 1996, A&A, 315, L333
Shenoy, S. S., Whittet, D. C. B., Ives, J. A., & Watson, D. M. 2008, ApJS, 176, 457
Skrutskie, M. F., et al. 2006, AJ, 131, 1163
Smith, R. G., Sellgren, K., & Brooke, T. Y. 1993, MNRAS, 263, 749
Tanaka, M., Sato, S., Nagata, T., & Yamamoto, T. 1990, ApJ, 352, 724
Thi, W., van Dishoeck, E. F., Dartois, E., Pontoppidan, K. M., Schutte, W. A., Ehrenfreund, P., d'Hendecourt, L., & Fraser, H. J. 2006, A&A, 449, 251
Tielens, A. G. G. M., Allamandola, L. J., Bregman, J., Goebel, J., Witteborn, F. C., & d'Hendecourt, L. B. 1984, ApJ, 287, 697
Tokunaga, A. T. 2000, in Infrared Astronomy, Allen's Astrophysical Quantities, ed. A. N. Cox (4th ed.; New York: Springer-Verlag), 143
Vacca, W. D., Cushing, M. C., & Rayner, J. T. 2003, PASP, 115, 389
van Breemen, J. M., et al. 2011, A&A, 526, A152
Wallace, L., & Hinkle, K. 1996, ApJS, 107, 312
Wallace, L., & Hinkle, K. 1997, ApJS, 111, 445
Werner, M. W., et al. 2004, ApJS, 154, 1
Whipple, F. L. 1950, ApJ, 111, 375
Whittet, D. C. B. 2003, Dust in the Galactic Environment (2nd ed.; Bristol: Institute of Physics Publishing)
Whittet, D. C. B., Adamson, A. J., Duley, W. W., Geballe, T. R., & McFadzean, A. D. 1989, MNRAS, 241, 707
Whittet, D. C. B., Bode, M. F., Longmore, A. J., Admason, A. J., McFadzean, A. D., Aitken, D. K., & Roche, P. F. 1988, MNRAS, 233, 321
Whittet, D. C. B., Cook, A. M., Chiar, J. E., Pendleton, Y. J., Shenoy, S. S., & Gerakines, P. A. 2009, ApJ, 695, 94
Whittet, D. C. B., Gerakines, P. A., Hough, J. H., & Shenoy, S. S. 2001, ApJ, 547, 872
Whittet, D. C. B., Shenoy, S. S., Bergin, E. A., Chiar, J. E., Gerakines, P. A., Gibb, E. L., Melnick, G. J., & Neufeld, D. A. 2007, ApJ, 655, 332
Williams, D. A., Hartquist, T. W., & Whittet, D. C. B. 1992, MNRAS, 258, 599